

# A Dual-Channel Pseudo-Differential CMOS AFE for Fluorescence Optical Fiber Temperature Measurement

Bingjun Xiong<sup>✉</sup>, Jingjing Liu<sup>✉</sup>, *Member, IEEE*, Jian Yang<sup>✉</sup>, Feng Yan<sup>✉</sup>, Xinying Su<sup>✉</sup>,  
and Yang Wang<sup>✉</sup>, *Member, IEEE*

**Abstract**—The escalating importance of temperature monitoring across industrial production, medical diagnostics, and environmental surveillance poses significant challenges for temperature sensing technologies, particularly in detection precision, electromagnetic interference resilience, and environmental adaptability. In response to these challenges, this article proposes an integrated solution for fluorescence optical fiber temperature sensors, based on a 0.18  $\mu\text{m}$  CMOS process. The proposed approach uses a dual-channel pseudo-differential analog frontend (AFE) based on a pre-current transimpedance amplifier (PC-TIA). The CMOS AFE employs a novel zero-bias single photodiode (PD) fluorescence detection architecture, enabling differential light detection from a single incident light beam. This results in improved system reliability and measurement accuracy. The proposed pre-current amplifier uses complementary transistors to achieve highly linear amplification of differential current signals. A transimpedance amplifier converts the amplified current into a voltage signal. By employing a dc offset cancellation (DCOC), it effectively solves the issues related to the dc offset voltage at the input stage and the dark current of the PD. Measurement results indicate that the proposed CMOS AFE circuit attains a transimpedance gain of 152.03  $\text{dB}\Omega$ , along with a  $-3$  dB bandwidth of 4 kHz and an input-referred noise (IRN) current spectral density of 56.3  $\text{fA}/\sqrt{\text{Hz}}$ . These parameters highlight the system's exceptional capability for high-precision temperature measurements. The prototype chip achieved a maximum differential output swing of 3.25  $\text{V}_{\text{pp,out}}$ , validated using both electrical and optical measurement setups. With a temperature range from  $-30$   $^{\circ}\text{C}$  to  $100$   $^{\circ}\text{C}$ , the proposed temperature sensor prototype exhibited an average error of  $-0.19$   $^{\circ}\text{C}$  and a measurement standard deviation of 0.29  $^{\circ}\text{C}$ .

**Index Terms**—Analog frontend (AFE), dual-channel, pseudo-differential, single photodiode (PD), temperature sensor.

## I. INTRODUCTION

TEMPERATURE monitoring plays a vital role in the industrial production, medical diagnosis, and environmental monitoring. Technological advances have led

to a growing demand for precise and reliable temperature measurements [1], [2], [3], [4]. Traditional thermocouples and thermistors use electrical signals for transmission, making them vulnerable to electromagnetic interference, which affects accuracy. They also present safety hazards in high voltage environments. In contrast, fluorescent optical fiber temperature sensors rely on optical signals for transmission, are highly resistant to electromagnetic interference, and are well-suited for harsh environments with strong electromagnetism, high pressure, flammability, and explosiveness [5], [6]. These sensors are suitable for long-distance, high-precision temperature monitoring tasks like temperature control in energy production, precision equipment monitoring, and real-time body temperature monitoring in clinical medicine. Fluorescence optical fiber temperature sensors employ three primary detection principles: intensity-based, intensity ratio-based, and fluorescence lifetime-based. The intensity-based approach is simple but susceptible to inaccuracies due to light source variations and fiber bending, especially in harsh environments, hindering high-precision measurements [7]. Conversely, the intensity ratio-based method seeks to enhance the accuracy beyond the intensity-based technique, but its complex fiber components increase costs without achieving optimal accuracy [8]. The fluorescence lifetime-based method measures temperature via fluorescence lifetime, unaffected by light source intensity and fiber bending, offering exceptional sensitivity and accuracy in low to mid-temperature ranges [9]. Considering the inherent stability and reliability of fluorescence lifetime as a temperature metric, this study has chosen fluorescence lifetime-based sensors for their substantial advantages in temperature measurement.

In CMOS analog frontend (AFE) circuits, traditional solutions typically involve connecting a dummy photodiode (PD) to the input of a differential (or pseudo-differential) TIA to generate a differential signal, as shown in Fig. 1(a). However, this method introduces additional noise, thereby reducing system sensitivity. In [10] and [11], two PDs are used for differential optical detection. However, this approach requires precise optical path alignment and relies on two differentially modulated light beams, which increases both system cost and complexity, as illustrated in Fig. 1(b). To enable differential light detection without a dummy input, a PD can be connected across the two input terminals of a TIA. However, maintaining the PD's reverse bias requires additional bias components, which increase noise. In [12] and [13], ac coupling is adopted to enable the PD to support differential

Received 24 March 2025; revised 25 April 2025; accepted 4 May 2025. Date of publication 27 May 2025; date of current version 5 June 2025. This work was supported by the National Natural Science Foundation of China under Grant 62174181 and Grant 62304007. The Associate Editor coordinating the review process was Dr. Sergio Rapuano. (Corresponding authors: Jingjing Liu; Yang Wang.)

Bingjun Xiong, Jingjing Liu, Feng Yan, and Xinying Su are with the School of Electronics and Communication Engineering, Sun Yat-sen University, Shenzhen 518107, China (e-mail: xiongjb@mail2.sysu.edu.cn; liujj77@mail.sysu.edu.cn; yanf9@mail2.sysu.edu.cn; suxy55@mail2.sysu.edu.cn).

Jian Yang is with the School of Physics and Electronics, Hunan Normal University, Changsha 410081, China (e-mail: 514625349@qq.com).

Yang Wang is with the College of Integrated Circuit Science and Engineering, Nanjing University of Posts and Telecommunications, Nanjing 210023, China (e-mail: wangyangjyz@njupt.edu.cn).

Digital Object Identifier 10.1109/TIM.2025.3573352

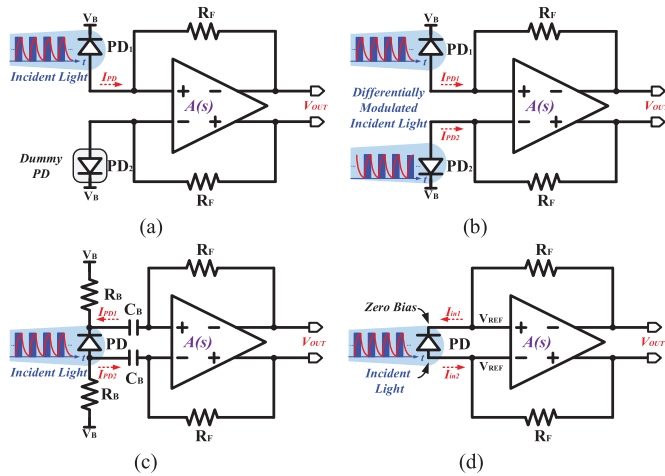


Fig. 1. Illustration of differential optical detection AFE architecture. (a) One detection PD with one dummy PD. (b) Dual detection PDs with two differential incident light beams. (c) One detection PD with a cross-connected structure based on ac coupling. (d) Proposed zero-bias detection PD with a single incident beam.

light detection while maintaining the appropriate reverse bias conditions, as depicted in Fig. 1(c). However, this approach requires a large coupling capacitance to mitigate signal loss. Additionally, the equivalent parasitic capacitance of the PD at each input terminal of the TIA is doubled, which limits both gain enhancement and noise performance improvement. The proposed structure, as shown in Fig. 1(d), removes the bias structure and coupling capacitors to improve circuit efficiency. Furthermore, implementing a zero-bias single-PD differential detection architecture further enhances noise performance. This approach also reduces design complexity and cost, making it more suitable for practical applications.

The remarkable temperature measurement capabilities of this technology have made it an excellent replacement for traditional active sensors such as thermocouples [14], [15]. Zhao et al. [16] developed a compact sensor with Mn<sup>4+</sup> doped fluorogermanate phosphors. The design integrates a three-way optical path, effectively separating fluorescence and achieving high accuracy with a 0.45 °C deviation [16]. Jiang et al. [17] designed a hybrid sensor for simultaneous temperature and pressure measurement, combining Fabry-Perot interferometry with fluorescent materials and achieving a sensitivity of 0.0048 ms/°C within 25 °C–80 °C. However, with ongoing advancements in integrated circuit technology, recent research has increasingly favored the use of integrated components to achieve more compact, reliable, and effective designs [18], [19], [20].

A notable trend emerged in utilizing advanced IC technologies, particularly CMOS, for AFE circuit development. The CMOS technology is favored for its low cost and power efficiency compared to SiGe or BiCMOS, allowing for smaller transistor sizes (3 nm) and reduced supply voltages (0.65 V) [21], which perfectly aligned with our design requirements [22], [23], [24], [25], [26], [27], [28], [29], [30], [31]. This article proposed a CMOS IC-based solution for the fluorescence temperature measurement system, reducing component count, optimizing signal matching paths, enhancing

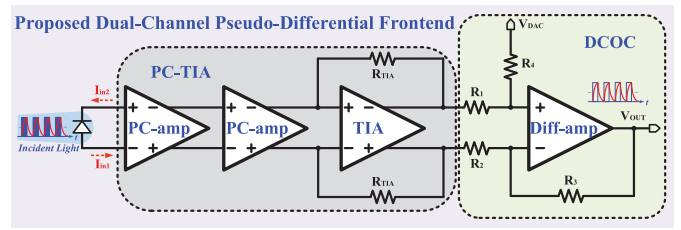


Fig. 2. Structure of the proposed dual-channel pseudo-differential frontend based on the PC-TIA.

the signal-to-noise ratio, and lowering system costs. This approach effectively overcame the limitations of traditional discrete systems, significantly improving detection accuracy.

A dual-channel pseudo-differential frontend architecture based on a pre-current transimpedance amplifier (PC-TIA) is proposed, as illustrated in Fig. 2. This design employs a zero-bias single-PD to achieve a differential light detection. It features two stages of pre-current amplifiers and one stage of a transimpedance amplifier. The pre-current amplifiers linearly amplify the photocurrent signal, while the transimpedance amplifier converts it into a voltage signal. Additionally, the dc offset cancellation (DCOC) structure, featuring a fully differential output stage, effectively eliminates both the dc offset and PD dark current. This CMOS AFE circuit can achieve nanoampere-level current detection and high transmission gain, demonstrating its excellent performance in temperature measurement applications. The rest of this article is organized as follows. Section II introduces the principle of the fluorescence optical fiber temperature sensors system. Section III introduces the proposed the CMOS AFE circuit. The experimental results and discussions are presented in Section IV. Section V concludes this article.

## II. PRINCIPLE OF THE FLUORESCENCE OPTICAL FIBER TEMPERATURE SENSOR SYSTEM

The basic components of fluorescence optical fiber temperature sensors include rare earth fluorescent materials, multimode quartz optical fibers, long-pass emission filters, near-ultraviolet LED and red light-sensitive PDs [23], [24]. The LED driver circuit modulates the LED, emitting pulsed excitation light with adjustable power, and employs an optical lens to focus the laser light into the multimode quartz optical fiber. Excitation of the rare earth fluorescent material by a purple LED ( $\lambda = 395$  nm) causes the electrons in the fluorescent molecules to jump to a higher energy state. Subsequently, these electrons return to their base state, emitting photons ( $\lambda = 620$  nm) detected by the PD. The lifetime ( $\tau$ ) of re-emitted 620 nm photons inversely correlates with external temperature, allowing for temperature determination through  $\tau$  measurement. Modern research measures photocurrent, indicator of photon intensity, and  $\tau$  using various AFEs.

### A. System Architecture

The proposed prototype of the fluorescence optical fiber temperature sensor comprises five main components as illustrated in Fig. 3.

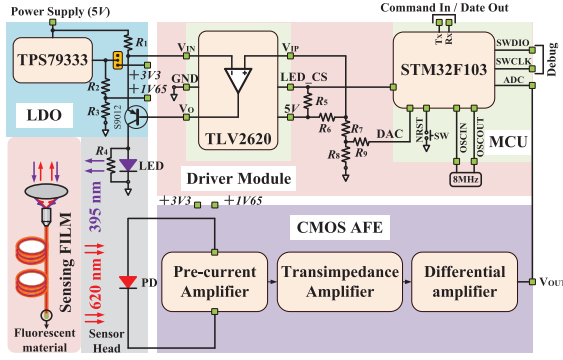


Fig. 3. Schematic of the proposed fluorescence optical fiber temperature sensor system.

- 1) The power management unit (LDO) distributes power among modules.
- 2) The driver module operates the LED.
- 3) The sensor head, containing fluorescent material, is optically excited and captures the material's optical response.
- 4) The CMOS AFE, linked to the sensor head, transforms the photocurrent from the PD into a photovoltage signal.
- 5) The STM32 MCU manages the LED driver, processes the fluorescence decay curve from the AFE to calculate the fluorescence lifetime (with an ADC sampling frequency of 1 MHz), converts it into temperature data, and transmits the data to an external device via a serial port.

The proposed sensor utilizes three power rails: a 5 V rail for the LED, a 3.3 V rail for the MCU and CMOS AFE, and a 1.65 V rail for the reference voltage ( $V_{REF}$ ) to the AFE. The LDO (TI's TPS79333) reduces the 5 V input to a stable 3.3 V output and provides a 1.65 V reference voltage. The LED driver module manages the periodic modulation and power adjustment of the LED light source. This modulation facilitates fast toggling of LED states, mitigating the effects of light source instability on the fluorescence decay curve. The LED, a current-mode device, shows strong linearity between its operating current, power, and the resultant fluorescence signal intensity. By adjusting the LED's current (ranging from 0 to 20 mA in 0.02 mA steps), both its power and the fluorescence intensity can be precisely controlled. The sensor head comprises an LED (peak wavelength: 395 nm) to excite fluorescent materials, and a PD (responsivity: 0.62 A/W) to detect signals at the 620 nm peak emission from these materials. The CMOS AFE, the focal point of this study, is fabricated using a 0.18  $\mu\text{m}$  CMOS process. It integrates a two-stage pre-current amplifier, a transimpedance amplifier, and a fully differential amplifier circuit. The dual-channel pseudo-differential configuration receives and amplifies the PD's photocurrent signal. Then the TIA transforms it into a voltage signal. A fully differential amplifier circuit processes the dual-channel outputs and generates  $V_{OUT}$ , which is corrected for dark current and dc level offsets.

### B. Technology for Estimating Fluorescence Lifetime

The principle of temperature measurement in fluorescence lifetime based optical fiber sensors involves two main steps.

- 1) *Excitation*: Upon activating the LED, fluorescence intensity increases until it peaks at  $I_0$ , at which point the LED is deactivated.
- 2) *Decay*: Post LED deactivation, fluorescence exponentially decays. This decay phase is crucial in rare earth fluorescence temperature measurement systems.

The expression for fluorescence intensity,  $I(t)$ , is as follows:

$$I(t) = I_0 \cdot e^{-\frac{t}{\tau}} \quad (1)$$

where  $I(t)$  represents the fluorescence intensity over time,  $I_0$  denotes the initial fluorescence intensity, and  $\tau$  is the fluorescence lifetime, representing the time required for the intensity to decay from  $I_0$  to  $I_0/e$ . The fluorescence lifetime is highly sensitive to the external temperature  $T$ . Then  $\tau$  can be obtained by (2) [24]

$$\tau = \Delta t / \ln(M) s \quad (2)$$

where  $\Delta t$  denotes the time interval utilized to segment the fluorescence decay curve into three equidistant portions.  $M$  represents the integral area ratio  $(S_1 - S_2)/(S_2 - S_3)$ , wherein  $S$  denotes the area. According to (2), the  $\tau$  depends solely on  $\Delta t$  and  $M$ . As an intrinsic property of the fluorescent material,  $\tau$  uniquely correlates with temperature.

### III. DUAL-CHANNEL PSEUDO-DIFFERENTIAL AFE CIRCUIT

The proposed dual-channel pseudo-differential AFE circuit is illustrated in Fig. 4. It has two symmetrical branches. The upper branch utilizes operational amplifiers  $OA_1$  and  $OA_2$  with units  $Z_1$  to  $Z_4$  to form a two-stage pre-current amplifier for direct photocurrent signal amplification. The proposed pre-current amplifier, based on complementary transistor units  $Z_s$  and subthreshold operation technique, suppresses the nonlinear voltage-current characteristics of the transistor through a symmetrical layout and feedback mechanism. For example, because two pairs of complementary transistors  $Z_1/Z_2$  operate at the same working point, and  $Z_2$  are paralleled  $N$  copies of  $Z_1$ , this configuration ensures the linear amplification of the differential current by  $N$  times, independent of the transistor's nonlinear voltage-current characteristics and any geometric dependence of the transistor parameters. Additionally, operating transistors in the sub-threshold range allows the amplifier to handle pA-level current.  $OA_3$  and  $R_{F1}$  constitute a transimpedance amplifier circuit for converting current to voltage.  $C_{F1}$ , a compensation capacitor, enhances TIA's stability. Similarly, compensation capacitors  $C_1$  to  $C_8$  are added to ensure feedback stability.

The proposed CMOS AFE features a dual-channel pseudo-differential receiving architecture, with the cathode and anode of the zero-bias single-PD device connected to the inverse input terminals of  $OA_1$  and  $OA_4$ , respectively. This zero-bias single-PD differential detection architecture can achieve differential optical detection of a single incident light beam, producing consistent differential current signals even under time-varying conditions. When incident light illuminates the single PD,  $I_{in1}$  and  $I_{in2}$  flow in the opposite directions, generating differential currents. The TIA converts the differential

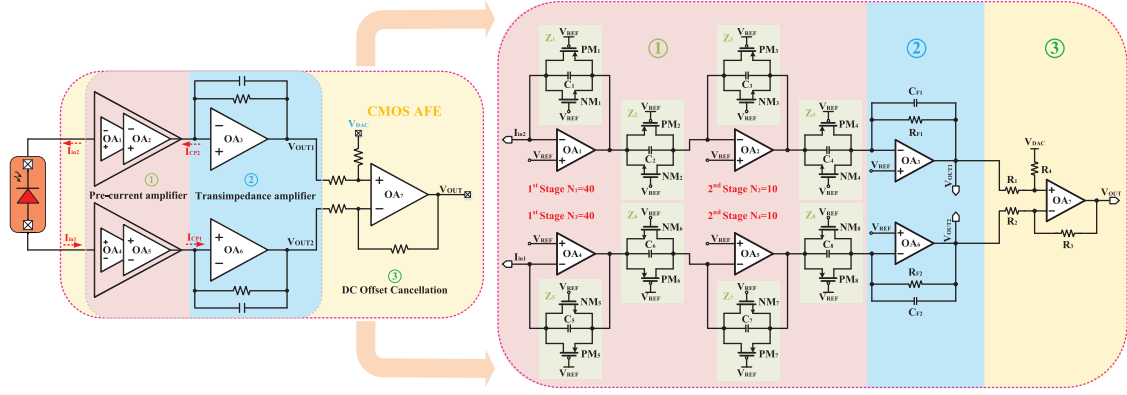


Fig. 4. Schematic of the proposed CMOS AFE circuit.

photocurrent into a voltage. Additionally, the proposed DCOC module not only suppresses shifts caused by the PD's dark current and circuit mismatches, but also subtracts the output voltages from the dual-channel CMOS AFE, which effectively doubles the target signal's amplitude. Finally, the  $V_{DAC}$  regulates the module's static operating point, allowing the final target signal to achieve a full-scale output without distortions.

The proposed pre-current amplifier, featuring operational amplifiers  $OA_1$ , units  $Z_1$  and  $Z_2$ , provides a linear photocurrent gain with an initial amplification factor of 40.  $Z_1$  and  $Z_2$  include pMOS and nMOS transistors, along with capacitors. To ensure linear photocurrent amplification,  $OA_1$ 's non-inverting input and all transistor gates are connected to the dc quiescent operating voltage  $V_{REF}$ , causing the drain voltage of  $PM_1$  and  $NM_1$  to be  $V_{REF}$ . Input current variations directly impact the source potential of MOSFETs. With  $Z_1$  and  $Z_2$  biased by operational amplifier feedback, and all MOSFET gates tied to  $V_{REF}$  with common source connections,  $Z_1$  and  $Z_2$  potentials uniformly adjust.  $Z_2$ 's width-to-length ratio is set as 40 times greater than  $Z_1$ 's size. The gate-source voltages of  $Z_1$  and  $Z_2$  are equal, it follows that:

$$\begin{aligned} mV_T \cdot \ln \left[ \frac{I_{DS\_Z1}}{\mu C_{ox} \cdot \left(\frac{W}{L}\right)_{Z1} \cdot V_T^2} \right] + V_{TH} \\ = mV_T \cdot \ln \left[ \frac{I_{DS\_Z2}}{40\mu C_{ox} \cdot \left(\frac{W}{L}\right)_{Z1} \cdot V_T^2} \right] + V_{TH} \end{aligned} \quad (3)$$

where  $I_{D\_Z1}$  denotes the drain current flowing through the transistor within the unit  $Z_1$ , whereas  $I_{D\_Z2}$  represents the drain current through the transistor in the unit  $Z_2$ . To maintain equal  $V_{GS}$  values, the circuit design requires the drain current through  $Z_2$  to be 40 times greater than through  $Z_1$ . Consequently

$$I_{DS\_Z2} = 40I_{DS\_Z1}A. \quad (4)$$

Applying this principle allows a  $40\times$  increase in current. By paralleling  $Z_2$  with  $Z_1$  in the layout design, linear current amplification is ensured, minimizing MOS mismatch errors. Similarly,  $Z_3$  and  $Z_4$  achieve an additional  $10\times$  secondary amplification. So the total gain of the pre-current amplifier is 400. The TIA circuit then transforms this amplified photocurrent into photovoltage through  $R_{F1}$  (100 k $\Omega$ ). To ease signal collection and processing, a differential amplifier with

unity gain subtracts the two branch signals. Consequently, the total transimpedance gain ( $R_T$ ) of the single-channel CMOS AFE is given by

$$R_T = \frac{I_{DS\_Z2}}{I_{DS\_Z1}} \cdot \frac{I_{DS\_Z4}}{I_{DS\_Z3}} \cdot R_{F1} \cdot 1 = 400R_{F1} \Omega. \quad (5)$$

If there is a current drawn from the pre-current amplifier inputs, the same mechanism works through the nMOS in the units  $Z_1 \sim Z_8$ .

When forward current  $I_{CP1}$  is applied, nMOS transistors  $NM_1$  and  $NM_2$  operate in the cutoff region, while pMOS transistors  $PM_1$  and  $PM_2$  are in the sub-threshold region. So the first stage's equivalent noise current primarily comes from a common gate amplifier circuit, with  $PM_1$  as the input and  $PM_2$  in diode connection as the load. Given the first-stage gain of  $N_1$ , the total input-referred current noise power is calculated as follows:

$$\bar{i}_{neq,CPam1}^2 \approx \frac{4kT}{N_1^2} \left( \gamma \cdot g_{PM1} + \frac{1}{g_{PM2}} \right) A^2/Hz \quad (6)$$

where  $g_{MP1}$  and  $g_{MP2}$  denotes the transconductance parameter of the transistor, and  $\gamma$  is the transistor excess noise factor. Given that  $g_{MP2} = 40g_{MP1}$ , (6) can be simplified to be

$$\bar{i}_{neq,CPam1}^2 \approx \frac{4kT}{N_1^2} \cdot \gamma \cdot g_{PM1} A^2/Hz. \quad (7)$$

Applying the same analysis to the CMOS AFE, and utilizing the superposition principle, the total equivalent input noise power can be determined as follows:

$$\begin{aligned} \bar{i}_{n,in}^2 &\approx \frac{4kT}{N_1^2} \cdot \gamma \cdot g_{PM1} + \frac{4kT}{N_1^2 \cdot N_2^2} \cdot \gamma \cdot g_{NM3} + \frac{4kT}{N_1^2 \cdot N_2^2 \cdot R_{F1}^3} \\ &\approx \frac{4kT}{N_1^2} \cdot \gamma \cdot g_{PM1} A^2/Hz. \end{aligned} \quad (8)$$

Noise from the final two stages is minimal, making the pre-current amplifier's first stage become the primary source of the equivalent input noise power.

The proposed two-stage pre-current amplifier circuit can precisely amplify input photocurrents ( $I_{PD}$ ) ranging from 0 to 300 nA by 400 times. Simulation results are depicted in Fig. 5 and reveal that at the  $I_{PD}$  of 50 pA, the maximum linear gain errors for  $I_{CP1}$  and  $I_{CP2}$  are 3.07% and 3.09%, respectively. When the input signal  $I_{in}$  is very weak, specifically at 50 pA, the complementary transistors in  $Z_1$  and  $Z_2$  transition from



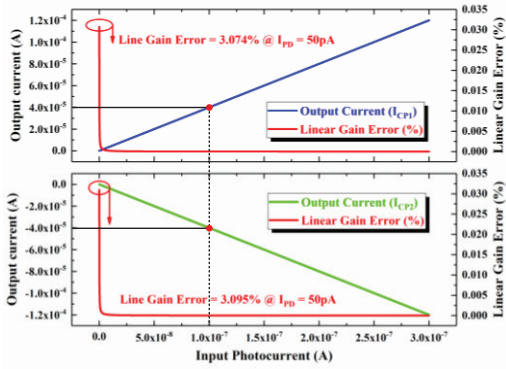


Fig. 5. Simulation results of the relationship between input current and output current for the proposed pre-current amplifier.

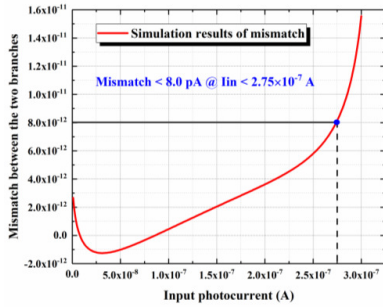


Fig. 6. Simulation results of the mismatch between the two branches.

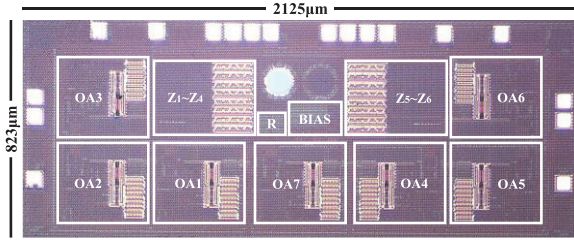


Fig. 7. Microscope image of the proposed CMOS AFE.

the cutoff region to the subthreshold region, resulting in a large gain error. As the input signal increases to between 1 and 300 nA, the transistors in  $Z_1$  and  $Z_2$  fully operate in the subthreshold region. During this period, the operating states of  $Z_1$  and  $Z_2$  are completely consistent, making the gain error almost negligible. Fig. 6 presents the mismatch simulation results between the two branches. It indicates that within the input current range of 0–275 nA, the maximum mismatch between the two branches is less than 8 pA. This suggests that the mismatch effect of the pseudo-differential paths is almost negligible. Thus, the proposed dual-channel pseudo-differential frontend not only provides a minimum resolution of 50 pA but also maintains minimal linear gain error across both channels. The linear gain error becomes negligible for higher photocurrent inputs within the nA range.

#### IV. EXPERIMENTAL RESULTS AND DISCUSSION

The proposed CMOS AFE is fabricated using a standard 180 nm CMOS process with an effective size of 2125 by 823  $\mu\text{m}$  and its microscope image is shown in Fig. 7. The chip is packaged within a DIP24 ceramic tube for simplified

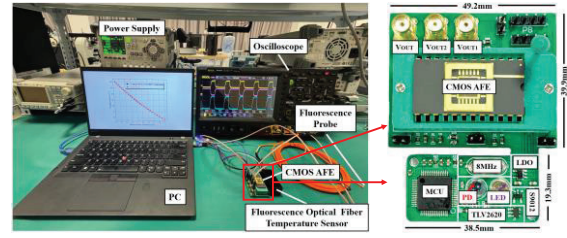


Fig. 8. Measurement platform and the prototype of the proposed fluorescence optical fiber temperature sensor.

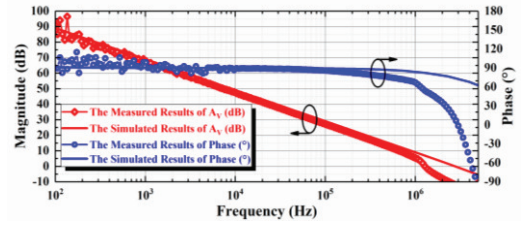


Fig. 9. Measurement results of the operational amplifier frequency response.

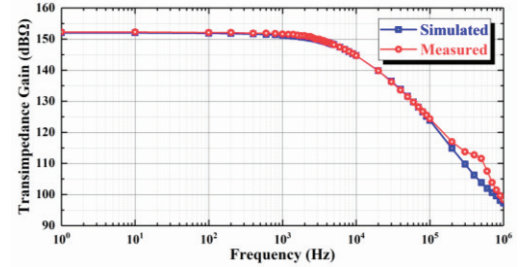


Fig. 10. Measurement results of single-channel CMOS AFE transimpedance gain.

testing. The prototype of the proposed fluorescence optical fiber temperature sensor and measurement platform is shown in Fig. 8. The system's prototype is including the CMOS AFE's PCB and the necessary peripheral signal processing module. They occupy an effective area of 39.9 by 49.2 mm and 19.3 by 38.5 mm, respectively.

The frequency response of the operational amplifier was measured using the Keysight Infiniivision X-Series oscilloscope's function/arbitrary waveform generator. A Picotest N2101A injection transformer isolated dc bias and ac interference, while a 1:1 passive probe minimized oscilloscope and switching noise, enhancing the signal-to-noise ratio. The measurement results are depicted in Fig. 9 and they indicate a gain of 91.02 dB, a phase margin of 57°, and a unity gain bandwidth of 1.21 MHz. To assess the CMOS AFE's frequency response, OA<sub>1</sub>'s inverting input was connected to the signal generator through a 10 M $\Omega$  resistor, while OA<sub>4</sub>'s inverting input remained unconnected. A RIGOL DG5352 arbitrary waveform generator produced a 0.2V<sub>pp</sub> sinusoidal  $V_{IN}$ , generating a 20 nA  $I_{CP1}$  through the off-chip resistor. The output  $V_{OUT}$  was displayed on a RIGOL MSO8204 oscilloscope. Altering the frequency of the 0.2V<sub>pp</sub> sinusoidal signal and recording  $V_{OUT}$  for the AFE, the transimpedance gain curve was obtained, as shown in Fig. 10. The CMOS AFE demonstrated a transimpedance gain of 152.03 dB $\Omega$  and a –3 dB bandwidth of 4 kHz.

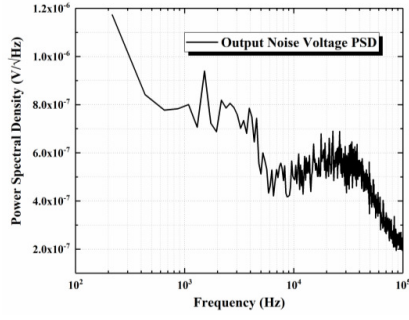


Fig. 11. Measurement results of the noise PSD for the proposed CMOS AFE.

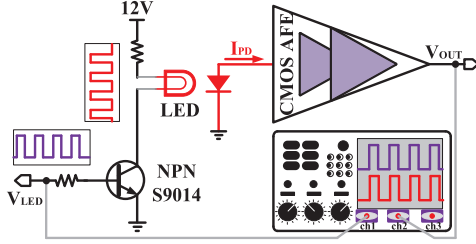


Fig. 12. Measurement setup for the transient response of the proposed AFE.

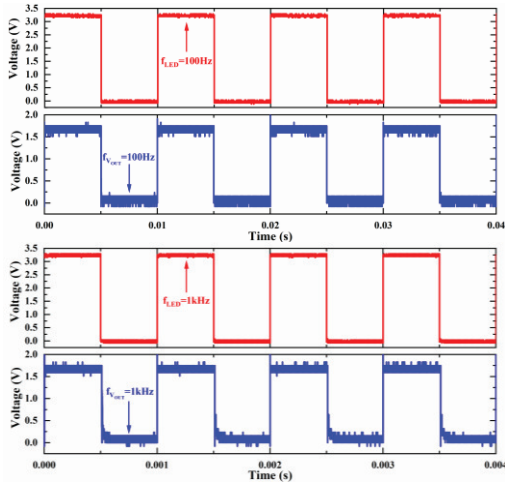


Fig. 13. Transient measurement results of the proposed CMOS AFE.

The noise spectrum was obtained by measuring the power spectral density (PSD) using a spectrum analyzer (KEYSIGHT N9322C) with the PD unexcited. The AFE output was connected to the spectrum analyzer to measure and record the total noise PSD curve. The measurement results are shown in Fig. 11. Based on these results, the integrated equivalent input-referred noise (IRN) PSD over the 100 kHz measurement frequency range is  $1.27 \times 10^{-23} \text{ A}^2/\text{Hz}$ . Average the integrated value over the AFE bandwidth frequency range (4 kHz) and take the square root of this average, the average equivalent IRN PSD can be obtained as shown in (9)

$$I_{n,\text{in,avg}} = \sqrt{1.27 \times 10^{-23} / 4000} = 56.3 \text{ fA} / \sqrt{\text{Hz}}. \quad (9)$$

To assess the transient response of the proposed fluorescent optical temperature sensor frontend circuit, an external LED driver provided a 3.3 V amplitude square wave signal to drive a 620 nm LED via transistor S9014 at various frequencies, as shown in Fig. 12. The output waveforms are free from distortion at lower frequencies like 100 Hz and begin to

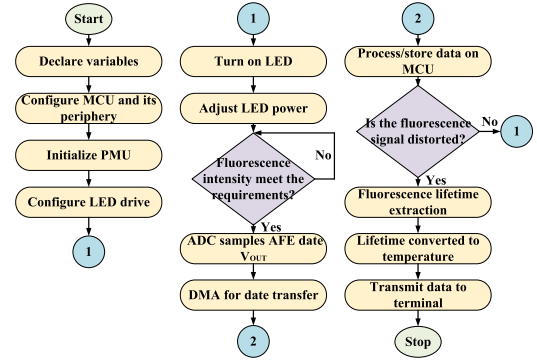


Fig. 14. Flowchart of main hardware logic.

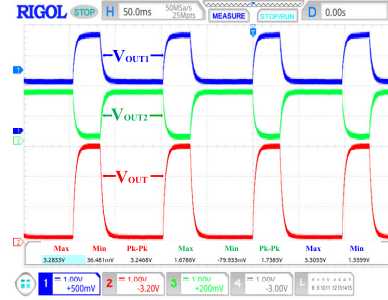


Fig. 15. Measurement results of the fluorescence signal.

show distortion at higher frequencies, e.g., 1 kHz, as captured in Fig. 13. However, the frequency remains adequate for detecting fluorescence decay signals [23].

Fig. 14 outlines the firmware logic of the proposed fluorescence optical fiber temperature sensor prototype, starting with MCU initialization (configuring the system clock, memory, ADC, DAC, timers, and interfaces). Contact is made with the LED driver via LED\_CS to adjust the LED current and thus the fluorescence intensity. Once adequate intensity is achieved, the MCU triggers the ADC to sample the  $V_{\text{OUT}}$  from the CMOS AFE. Subsequently, the sampled data undergoes high-speed transmission facilitated by direct memory access (DMA). The main loop assesses any distortion in the fluorescence decay signal, adjusting the DAC output to correct signal saturation or distortion. With minimal distortion, the MCU records the decay curve to calculate the fluorescence lifetime  $\tau$ , subsequently converting it to the temperature.

The proposed dual-channel cross-group output voltages  $V_{\text{OUT1}}$ ,  $V_{\text{OUT2}}$ , and the final output voltage  $V_{\text{OUT}}$  of the CMOS AFE were measured, with continuous adjustments made to the LED's operating current to optimize the fluorescence signal, as depicted in Fig. 15. Through fine-tuning, a robust fluorescence signal with a 3.25 V peak-to-peak value was achieved, facilitating accurate lifetime determination by the signal processing system. It can be obtained that the period of the fluorescence signal is 100 ms, and the ADC in the MCU operates at a sampling frequency ( $f_s$ ) of 1 MHz. As a result, each temperature measurement requires 100 000 sampling cycles ( $N$ ). The conversion time of the proposed temperature sensor is calculated as follows:

$$T_{\text{conv}} = N / f_s = 100 \text{ ms}. \quad (10)$$

To activate the prototype's external temperature detection capability, a comprehensive temperature calibration must be

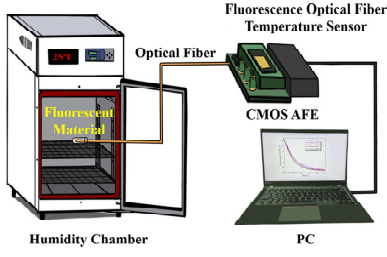


Fig. 16. Experimental setup for temperature sensing characterization.

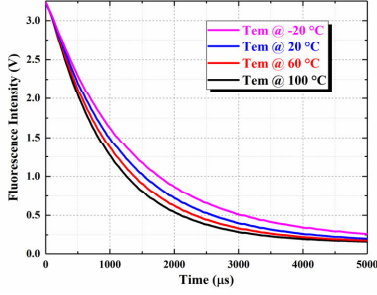


Fig. 17. Fluorescence decay curves collected at various temperatures.

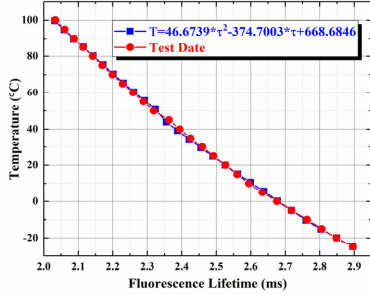


Fig. 18. Relationship between fluorescence lifetime and external temperature changes.

performed. This involves recording fluorescence lifetimes at standardized temperatures to derive the relationship between fluorescence lifetime and temperature. Multiple calibrations are essential to minimize random errors. The calibration setup includes a precise temperature and humidity chamber ( $\pm 0.01^\circ\text{C}$ ), the fluorescence optical fiber temperature sensor prototype, and a PC. Fig. 16 displays the setup for the temperature sensing experiments. Initially, set the chamber's temperature to  $-30^\circ\text{C}$ . Upon stabilization, the prototype operates and captures the fluorescence signal. The CMOS AFE's output goes through the ADC and MCU for fluorescence lifetime extraction, which is then automatically logged by the PC.

To minimize experimental errors, we measured fluorescence lifetimes 400 times at each temperature point and calculated the average. The temperature was incrementally raised from  $-30^\circ\text{C}$  to  $100^\circ\text{C}$ , with measurements taken every  $5^\circ\text{C}$ . Fig. 17 displays the decay curves at  $-20^\circ\text{C}$ ,  $20^\circ\text{C}$ ,  $60^\circ\text{C}$ , and  $100^\circ\text{C}$  respectively. Based on the measured decay curves and (3), the relationship between fluorescence lifetime and external temperature can be determined, as shown in Fig. 18. The fluorescence lifetime  $\tau$  decreases with rising temperature  $T$ , consistent with established theories. The data points exhibit good linearity with the fit curve. Calibration experiments

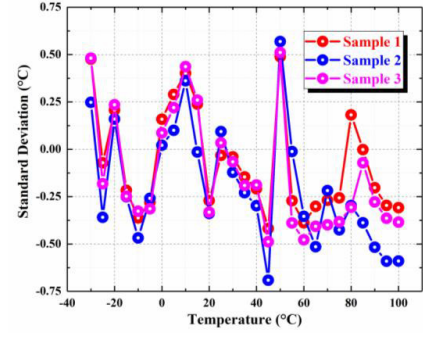


Fig. 19. Standard temperature error measured by three CMOS AFE sample chips.

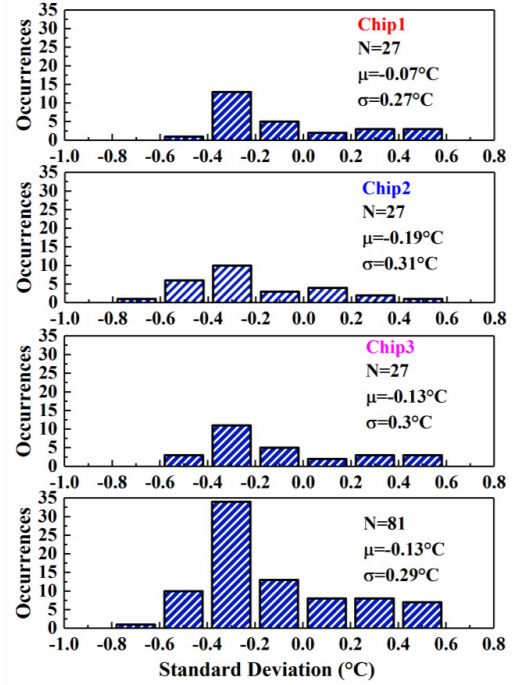


Fig. 20. Statistical results of standard temperature errors of three chips.

TABLE I  
PERFORMANCE SUMMARY AND COMPARISON WITH AFE CIRCUIT

	This work	SJ'20 <sup>[20]</sup>	JSTS'17 <sup>[22]</sup>	SJ'24 <sup>[23]</sup>	VLSI'17 <sup>[25]</sup>
<b>Technology</b>	180 nm	130 nm	110 nm	180 nm	130 nm
<b>Supply</b>	3.3 V	1.2 V	1.5 V	3.3 V	3.3 V
<b>Gain</b>	152.03 dBΩ	98.6 dBΩ	99.7 dBΩ	120.23 dBΩ	170 dBΩ
<b>Bandwidth</b>	4 kHz	43.3 kHz	4.2 kHz	6.7 kHz	1 MHz
<b>IRN PSD</b>	56.3 fA/√Hz	1.19 pA/√Hz	1.35 pA/√Hz	8.79 pA/√Hz	52 pA/√Hz
<b>Power</b>	3.86 mW	2.16 mW	2.1 mW	1.12 mW	30 mW
<b>Area</b>	1.74 mm <sup>2</sup>	2.2 mm <sup>2</sup>	0.22 mm <sup>2</sup>	0.25 mm <sup>2</sup>	0.2 mm <sup>2</sup>
<b>FoM</b>	1608.2	754.9	671.4	327.3	544.8

reveal a quadratic relationship between  $\tau$  and  $T$

$$T = (46.6739\tau^2 - 374.7003\tau + 668.6846)^\circ\text{C}. \quad (11)$$

To assess the temperature measurement accuracy of the proposed prototype, the temperature and humidity chamber are used to make each constant temperature test. The PC is used to calculate the temperature from (11) and compare it with the chamber temperature. Fig. 19 illustrates the prototype's temperature measurement errors, which is the discrepancy between prototype readings and the chamber's standard temperatures. To minimize the random errors, 400 temperature



readings at each standard temperature point were averaged. Fig. 20 presents statistical measurements from three CMOS AFE sample chips. Chip 1 demonstrates the highest accuracy across all temperatures, with an average error of  $-0.07^\circ\text{C}$  and a standard deviation of  $0.27^\circ\text{C}$ . The worst case is chip 2 and it shows an average error of  $-0.19^\circ\text{C}$  and the highest standard deviation of  $0.31^\circ\text{C}$ . Aggregating data from all three samples indicates an overall average temperature measurement error of  $-0.19^\circ\text{C}$  and a standard deviation of  $0.29^\circ\text{C}$  for the prototype. Table I shows the performance comparison of the proposed frontend circuit with others work. For fairly comparing the performance among the works, a figure of merit (FoM) is defined based on [30] as follows:

$$\text{FoM} = \frac{\text{Gain (dB}\Omega) \cdot \text{BW (kHz)}}{\text{IRN (pA}/\sqrt{\text{Hz}}) \cdot \text{Power (mW)} \cdot \text{Area (mm}^2\text{)}}. \quad (12)$$

The guide to the expression of uncertainty in measurement (GUM) employs the uncertainty propagation law to quantify uncertainty [31]. The uncertainty in measurement accuracy of the fluorescence optical fiber temperature sensor proposed in this article is primarily influenced by three factors: errors in fluorescence lifetime measurement caused by AFE noise, ambient temperature drift errors, and random errors in experimental measurements. From (9), the average equivalent IRN PSD of the proposed AFE is  $56.3 \text{ fA}/\sqrt{\text{Hz}}$ , and the bandwidth is  $4 \text{ kHz}$ . Consequently, the equivalent current noise  $i_{\text{eq}}$  is calculated as follows:

$$i_{\text{eq}} = 56.3 \times 10^{-15} \times \sqrt{4000} = 3.56 \text{ pA}. \quad (13)$$

When extracting the lifetime value from the fluorescence decay curve, the signal contains both the true fluorescence and noise. This noise introduces measurement errors, especially in the calculation of the integral area. It is assumed that the noise in each integral area is due to system noise. The variance of the noise current is proportional to the integration time  $\Delta t$ . Thus, the measurement uncertainty  $u(S)$  of the integral area is

$$u(S) = i_{\text{eq}} \cdot \sqrt{\Delta t}. \quad (14)$$

The integral area ratio  $M$  is determined using three distinct regions, with noise from these regions propagating into the calculation of  $M$ . Assuming that the noise in each region is independent and has an equal variance, the measurement uncertainty for the integral area ratio  $u(M)$  can be expressed as

$$u(M) \approx \sqrt{3} \times \frac{i_{\text{eq}} \cdot \sqrt{\Delta t}}{i_{\text{signal}} \cdot \Delta t} = \frac{\sqrt{3}}{\text{SNR} \cdot \sqrt{\Delta t}}. \quad (15)$$

The signal current  $i_{\text{signal}}$  is approximately  $40 \text{ nA}$ , with an SNR of 11236 (81 dB). As illustrated in Fig. 17, the fluorescence decay time is  $5 \text{ ms}$ , leading to  $\Delta t$  being  $1.67 \text{ ms}$ . Furthermore, the fluorescence lifetime  $\tau$  is  $2.49 \text{ ms}$  at room temperature ( $25^\circ\text{C}$ ). By substituting these values into (2),  $M$  is calculated to be approximately 1.955. According to the GUM error propagation formula [31], the uncertainty in the fluorescence lifetime  $u_{\text{AFE}}(\tau)$  is given by

$$u_{\text{AFE}}(\tau) = \left| \frac{\partial \tau}{\partial M} \right| u(M) = \frac{\sqrt{3}\Delta t}{M(\ln M)^2} \cdot \frac{1}{\text{SNR}} = 0.2267 \mu\text{s}. \quad (16)$$

TABLE II

PERFORMANCE SUMMARY AND COMPARISON WITH TEMPERATURE SENSORS

	This work	JSSC'23 <sup>[26]</sup>	JSSC'24 <sup>[27]</sup>	TCASI'20 <sup>[28]</sup>	TCASII'24 <sup>[29]</sup>
Technology (nm)	180	180	180	65	180
Supply (V)	3.3	1.4	1.8	1.3	2
T. Range ( $^\circ\text{C}$ )	-30 to 100	-55 to 125	-50 to 100	-10 to 110	-40 to 75
Tconv (ms)	100	128	0.08	4.1	0.01
Res. [ $^\circ\text{C}$ ]	0.0358	0.0018	0.092	0.065	0.104
Accuracy	0.29	0.45	1.96	2.64	1

The constant temperature and humidity chamber used in this study has an error of  $\pm 0.01^\circ\text{C}$ . Thus, the uncertainty due to ambient temperature drift  $u_{\text{Tem}}(T)$  can be estimated using a uniform distribution

$$u_{\text{Tem}}(T) = \frac{0.01}{\sqrt{3}} \approx 0.0058^\circ\text{C}. \quad (17)$$

As illustrated in Fig. 19, the proposed temperature sensor prototype achieved a measurement standard deviation of  $0.29^\circ\text{C}$ , with 400 data points collected at each temperature. Therefore, the uncertainty of random error propagation in chip sample measurement  $u_{\text{Random}}(T)$  is calculated as follows:

$$u_{\text{Random}}(T) = \frac{0.29}{\sqrt{400}} = 0.0145^\circ\text{C}. \quad (18)$$

Sensitivity  $s$  is defined as the change in fluorescence lifetime resulting from a unit change in temperature. From (11),  $s$  can be calculated as follows:

$$s = 1 \left/ \frac{dT}{d\tau} \right. \approx -7.029 \mu\text{s}/^\circ\text{C}. \quad (19)$$

It indicates that the fluorescence lifetime changes by approximately  $7.029 \mu\text{s}$  for each  $1^\circ\text{C}$  change in temperature. The negative sign represents a negative correlation between temperature and fluorescence lifetime; as temperature increases, the fluorescence lifetime decreases. Consequently, the temperature measurement uncertainty introduced by AFE noise  $u_{\text{AFE}}(T)$  can be calculated as follows:

$$u_{\text{AFE}}(T) = u_{\text{AFE}}(\tau)/|s| = 0.03225^\circ\text{C}. \quad (20)$$

According to the GUM propagation formula, the combined uncertainty  $u(T)$  (resolution) can be calculated as follows, with each uncertainty component being independent:

$$u(T) = \sqrt{[u_{\text{AFE}}(T)]^2 + [u_{\text{Tem}}(T)]^2 + [u_{\text{Random}}(T)]^2} \approx 0.0358^\circ\text{C}. \quad (21)$$

Thus, when the coverage factor  $k = 2$  (representing a 95% confidence interval), the expanded uncertainty  $U$  is

$$U = 2u(T) = 2 \times 0.0358^\circ\text{C} = 0.0716^\circ\text{C}. \quad (22)$$

In Table I, it is evident that the FoM of the proposed CMOS AFE circuit surpasses other works. This work demonstrates competitive features, particularly in noise performance, where it shows significant advantages. Additionally, Table II compares the temperature sensor's performance with that of state-of-the-art works. The results clearly show that the temperature sensor developed using the proposed CMOS AFE circuit achieves notable improvements in measurement accuracy. In summary, both the CMOS AFE circuit and the fluorescence optical fiber temperature sensor exhibit competitive performance in terms of noise and accuracy.



## V. CONCLUSION

This article proposed a dual-channel pseudo-differential AFE circuit using a 0.18  $\mu\text{m}$  CMOS process. It includes a pre-current amplifier for linear photocurrent amplification, a transimpedance amplifier for photovoltage signal conversion, and a DCOC structure effectively eliminates both the dc offset and PD dark current. Measurements indicate a 152.03 dB $\Omega$  transimpedance gain, a  $-3$  dB bandwidth of 4 kHz, and an IRN current spectral density of 56.3 fA/ $\sqrt{\text{Hz}}$ . The temperature sensor prototype's testing within  $-30$   $^{\circ}\text{C}$  to  $100$   $^{\circ}\text{C}$  revealed an average temperature error of  $-0.19$   $^{\circ}\text{C}$  and a standard deviation of  $0.29$   $^{\circ}\text{C}$ . Silicon-based optical sensors are now predominant in optoelectronic integrated circuits, favored for their low manufacturing costs and potential for dense integration. The proposed dual-channel pseudo-differential AFE circuit can be used for the high-precision fluorescence optical fiber temperature sensor applications.

## REFERENCES

- [1] H. Chen et al., "Integrated lateral SBD temperature sensor of a 4H-SiC VDMOS for real-time temperature monitoring," *IEEE Trans. Electron Devices*, vol. 70, no. 7, pp. 3813–3819, Jul. 2023, doi: [10.1109/TED.2023.3278624](#).
- [2] H. Yang, Y. Chen, Y. Shang, C. Yu, and Y. Kang, "A temperature monitoring method for power electronic converter based on infrared image and object detection algorithm," *IEEE Trans. Ind. Appl.*, vol. 59, no. 1, pp. 1090–1099, Jan. 2023, doi: [10.1109/TIA.2022.3208225](#).
- [3] Q. Zhang, G. Lu, Y. Yang, and P. Zhang, "A high-frequency online junction temperature monitoring method for SiC MOSFETs based on on-state resistance with aging compensation," *IEEE Trans. Ind. Electron.*, vol. 70, no. 7, pp. 7393–7405, Jul. 2023, doi: [10.1109/TIE.2022.3204948](#).
- [4] F. Yan and J. Liu, "Analog front-end input-impedance boosting techniques for bio-potential Monitoring—A review," *IEEE Trans. Instrum. Meas.*, vol. 73, pp. 1–14, 2024, doi: [10.1109/TIM.2024.3370766](#).
- [5] W. Wang et al., "Quantum dots-based multiplexed fiber-optic temperature sensors," *IEEE Sensors J.*, vol. 16, no. 8, pp. 2437–2441, Apr. 2016, doi: [10.1109/JSEN.2016.2516099](#).
- [6] B. Li et al., "Fluorescent optical fiber intensity ratio temperature sensor based on polymer matrix using down-conversion from ZnS: Cu," *IEEE Trans. Instrum. Meas.*, vol. 71, pp. 1–7, 2022, doi: [10.1109/TIM.2022.3198760](#).
- [7] Y. Fu, W. Li, and M. Huang, "Ultrawide range of concentration measurement assisted by fluorescence intensity distribution imaging," *IEEE Trans. Instrum. Meas.*, vol. 72, pp. 1–6, 2023, doi: [10.1109/TIM.2023.3308254](#).
- [8] W. Liu et al., "A reliable anti-interference probe based on fluorescence intensity ratio technique for cryogenic temperature detection," *J. Lightw. Technol.*, vol. 40, no. 21, pp. 7219–7225, Nov. 1, 2022, doi: [10.1109/JLT.2022.3200387](#).
- [9] O. Harbater, M. Ben-David, and I. Gannot, "Fluorescence lifetime and depth estimation of a tumor site for functional imaging purposes," *IEEE J. Sel. Topics Quantum Electron.*, vol. 16, no. 4, pp. 981–988, Jul. 2010, doi: [10.1109/JSTQE.2009.2033209](#).
- [10] M. G. Ahmed, T. N. Huynh, C. Williams, Y. Wang, P. K. Hanumolu, and A. Rylyakov, "34-GBd linear transimpedance amplifier for 200-Gb/s DP-16-QAM optical coherent receivers," *IEEE J. Solid-State Circuits*, vol. 54, no. 3, pp. 834–844, Mar. 2019, doi: [10.1109/JSSC.2018.2882265](#).
- [11] N. Mehta, S. Lin, B. Yin, S. Moazeni, and V. Stojanovic, "A laser-forwarded coherent transceiver in 45-nm SOI CMOS using monolithic microring resonators," *IEEE J. Solid-State Circuits*, vol. 55, no. 4, pp. 1096–1107, Apr. 2020, doi: [10.1109/JSSC.2020.2968764](#).
- [12] S. Kurtti, J. Nissinen, and J. Kostamovaara, "A wide dynamic range CMOS laser radar receiver with a time-domain walk error compensation scheme," *IEEE Trans. Circuits Syst. I, Reg. Papers*, vol. 64, no. 3, pp. 550–561, Mar. 2017, doi: [10.1109/TCSI.2016.2619762](#).
- [13] Y. Yang et al., "An on-chip AC coupled AFE with asymmetric output stage for d-ToF LiDAR," *IEEE Trans. Circuits Syst. II, Exp. Briefs*, vol. 72, no. 1, pp. 148–152, Jan. 2025, doi: [10.1109/TCSII.2024.3489640](#).
- [14] Y. Yang et al., "Packaged temperature sensor based on fluorescent microsphere with an embedded fiber microlens," *IEEE Photon. Technol. Lett.*, vol. 35, no. 8, pp. 398–401, Apr. 15, 2023, doi: [10.1109/LPT.2023.3250271](#).
- [15] D. Zhong et al., "An Er<sup>3+</sup>/Yb<sup>3+</sup> co-doped tellurite temperature sensor based on fluorescence intensity ratio technology for real-time thermal monitoring of automotive 3-D LiDAR," *IEEE Sensors J.*, vol. 23, no. 21, pp. 25895–25902, Nov. 2023, doi: [10.1109/JSEN.2023.3314092](#).
- [16] Y. Zhao, M.-Q. Chen, R.-Q. Lv, P. Wang, and X. Feng, "Small and practical optical fiber fluorescence temperature sensor," *IEEE Trans. Instrum. Meas.*, vol. 65, no. 10, pp. 2406–2411, Oct. 2016, doi: [10.1109/TIM.2016.2575241](#).
- [17] X. Jiang et al., "Hybrid fiber optic sensor, based on the Fabry-Pérot interference, assisted with fluorescent material for the simultaneous measurement of temperature and pressure," *Sensors*, vol. 19, no. 5, p. 1097, Mar. 2019, doi: [10.3390/s19051097](#).
- [18] A. Baharmast, S. Kurtti, and J. Kostamovaara, "A wide dynamic range laser radar receiver based on input pulse-shaping techniques," *IEEE Trans. Circuits Syst. I, Reg. Papers*, vol. 67, no. 8, pp. 2566–2577, Aug. 2020, doi: [10.1109/TCSI.2020.2983834](#).
- [19] X. Wang, R. Ma, D. Li, H. Zheng, M. Liu, and Z. Zhu, "A low walk error analog front-end circuit with intensity compensation for direct ToF LiDAR," *IEEE Trans. Circuits Syst. I, Reg. Papers*, vol. 67, no. 12, pp. 4309–4321, Dec. 2020, doi: [10.1109/TCSI.2020.3022714](#).
- [20] Y. He, J.-H. Kim, and S. M. Park, "A CMOS read-out IC for cyanobacteria detection with 40 nApp sensitivity and 45-dB dynamic range," *IEEE Sensors J.*, vol. 20, no. 8, pp. 4283–4289, Apr. 2020, doi: [10.1109/JSEN.2019.2962858](#).
- [21] A. Chowdhury et al., "A 0.9pj/b 9.8–113Gb/s XSR SerDes with 6-tap TX FFE and AC coupling RX in 3nm FinFet technology," in *Proc. IEEE Symp. VLSI Technol. Circuits (VLSI Technol. Circuits)*, Honolulu, HI, USA, Jun. 2024, pp. 1–2, doi: [10.1109/vlsitechnologyandcir46783.2024.10631354](#).
- [22] Y. He and S. M. Park, "Portable cyanobacteria detection fluorometer with current-conveyor transimpedance amplifiers," *J. Semicond. Technol. Sci.*, vol. 17, no. 6, pp. 886–892, Dec. 2017, doi: [10.5573/jsts.2017.17.6.886](#).
- [23] B. Xiong et al., "An integrated fluorescence optical fiber temperature sensor front-end based on a Ring-Gate-Isolated photodiode," *IEEE Sensors J.*, vol. 24, no. 8, pp. 12276–12285, Apr. 2024, doi: [10.1109/JSEN.2024.3369050](#).
- [24] J. Yang, Y. Wang, X. Jin, Y. Peng, and J. Luo, "A novel high precision weighted integral ratio algorithm for fluorescent optical fiber temperature sensor," *Opt. Quantum Electron.*, vol. 54, no. 1, pp. 1–14, Jan. 2022, doi: [10.1007/s11082-021-03401-0](#).
- [25] M. Taherzadeh-Sani, S. M. Hussain Hussaini, H. Rezaee-Dehsorkh, F. Nabki, and M. Sawan, "A 170-dB  $\Omega$  CMOS TIA with 52-pA input-referred noise and 1-MHz bandwidth for very low current sensing," *IEEE Trans. Very Large Scale Integr. (VLSI) Syst.*, vol. 25, no. 5, pp. 1756–1766, May 2017, doi: [10.1109/TVLSI.2017.2654452](#).
- [26] Z. Tang, S. Pan, M. Grubor, and K. A. A. Makinwa, "A Sub-1 v capacitively biased BJT-based temperature sensor with an inaccuracy of  $\pm 0.15$   $^{\circ}\text{C}$  (3 $\sigma$ ) From  $-55$   $^{\circ}\text{C}$  to  $125$   $^{\circ}\text{C}$ ," *IEEE J. Solid-State Circuits*, vol. 58, no. 12, pp. 3433–3441, Dec. 2023, doi: [10.1109/JSSC.2023.3308554](#).
- [27] A. Aprile, M. Folz, D. Gardino, P. Malcovati, and E. Bonizzoni, "An area-efficient smart temperature sensor based on a fully current processing error-feedback noise-shaping SAR ADC in 180-nm CMOS," *IEEE J. Solid-State Circuits*, vol. 59, no. 3, pp. 716–727, Mar. 2024, doi: [10.1109/JSSC.2023.3342937](#).
- [28] O. Bass and J. Shor, "A miniaturized 0.003 mm<sup>2</sup> PNP-based thermal sensor for dense CPU thermal monitoring," *IEEE Trans. Circuits Syst. I, Reg. Papers*, vol. 67, no. 9, pp. 2984–2992, Sep. 2020, doi: [10.1109/TCSI.2020.2987595](#).
- [29] H. Liu et al., "An ultra-high linear digitization temperature sensor based on SAR ADC with common-mode temperature drift suppression," *IEEE Trans. Circuits Syst. II, Exp. Briefs*, vol. 71, no. 3, pp. 1047–1051, Mar. 2024, doi: [10.1109/TCSII.2023.3316013](#).
- [30] Z. Zhang et al., "A wideband low-noise linear LiDAR analog front-end achieving 1.6-GHz bandwidth, 2.7-pA/Hz<sup>0.5</sup> input-referred noise, and 103-dB $\Omega$  transimpedance gain," *IEEE Solid-State Circuits Lett.*, vol. 7, pp. 131–134, 2024, doi: [10.1109/LSSC.2024.3378093](#).
- [31] R. Morello, "GUM-based decisional criteria to make decisions in presence of measurement uncertainty," *IEEE Trans. Instrum. Meas.*, vol. 69, no. 8, pp. 5511–5522, Aug. 2020, doi: [10.1109/TIM.2019.2963581](#).